JACS
JOURNAL OF THE AMERICAN CHEMICAL SOCIETY

Article

pubs.acs.org/JACS

Molecular Cobalt Complexes with Pendant Amines for Selective Electrocatalytic Reduction of Carbon Dioxide to Formic Acid

Souvik Roy,[†,#] Bhaskar Sharma,[‡] Jacques Pécaut,[§] Philippe Simon,[∥] Marc Fontecave,[∥] Phong D. Tran,[†,⊥] Etienne Derat,[‡] and Vincent Artero*[,†]

[†]Laboratoire de Chimie et Biologie des Métaux, Université Grenoble Alpes, CEA, CNRS, 17 rue des Martyrs, 38000 Grenoble, France

[‡]Institut Parisien de Chimie Moléculaire, UMR 8232, Sorbonne Universités, UPMC Univ. Paris 06, CNRS, 75005 Paris, France

[§]Reconnaissance Ionique et Chimie de Coordination, DRF-INAC-SyMMES, Université Grenoble Alpes, CNRS, CEA, 17 rue des Martyrs, 38000 Grenoble, France

[∥]Laboratoire de Chimie des Processus Biologiques, Collège de France, Université Pierre et Marie Curie, CNRS UMR 8229, 11 place Marcelin Berthelot, 75005 Paris, France

[⊥]Department of Advanced Materials Science and Nanotechnology, University of Science and Technology of Hanoi, Vietnam Academy of Science and Technology, 18 Hoang Quoc Viet, Cau Giay, 122102 Hanoi, Vietnam

Supporting Information

ABSTRACT: We report here on a new series of CO_2-reducing molecular catalysts based on Earth-abundant elements that are very selective for the production of formic acid in dimethylformamide (DMF)/water mixtures (Faradaic efficiency of 90 ± 10%) at moderate overpotentials (500−700 mV in DMF measured at the middle of the catalytic wave). The $[CpCo(P^R_2N^{R'}_2)I]^+$ compounds contain diphosphine ligands, $P^R_2N^{R'}_2$, with two pendant amine residues that act as proton relays during CO_2-reduction catalysis and tune their activity. Four different $P^R_2N^{R'}_2$ ligands with cyclohexyl or phenyl substituents on phosphorus and benzyl or phenyl substituents on nitrogen were employed, and the compound with the most electron-donating phosphine ligand and the most basic amine functions performs best among the series, with turnover frequency >1000 s^{-1}. State-of-the-art benchmarking of catalytic performances ranks this new class of cobalt-based complexes among the most promising CO_2-to-formic acid reducing catalysts developed to date; addressing the stability issues would allow further improvement. Mechanistic studies and density functional theory simulations confirmed the role of amine groups for stabilizing key intermediates through hydrogen bonding with water molecules during hydride transfer from the Co center to the CO_2 molecule.

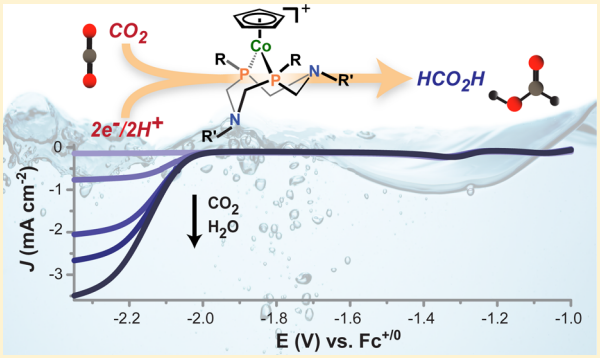

INTRODUCTION

Utilization of CO_2 as an economical and renewable C_1 feedstock for production of energy-dense carbon-based liquid and gaseous fuels is emerging as a particularly appealing strategy in the context of developing new energy storage technologies. CO_2 is a quite inert molecule that can only be activated through kinetically constrained multielectron/multiproton processes. Therefore, much research has been devoted to developing efficient and scalable catalysts for CO_2 reduction. However, despite promising results, many of these catalysts operate sluggishly, with low energy efficiencies and/or poor product selectivity. Molecular homogeneous catalysts contrast with their heterogeneous counterparts since they usually display high selectivity, but the most effective ones are often based on rare-earth metals (ruthenium, rhodium, rhenium, and iridium).[1,2] Consequently, more work must be done on the development on molecular catalysts using Earth-abundant elements.[3−6] Among the products formed upon electrochemical CO_2 reduction, CO and formic acid are the most economically viable ones.[7] Formic acid is a valuable chemical, derived from $2e^-$ reduction of CO_2, which can serve as a suitable energy carrier,[8] a hydrogen storage material,[9] a liquid fuel in formic acid fuel cell applications,[10] or a raw material for bacteria to generate higher alcohols as liquid fuels.[11] In nature, CO-dehydrogenases (CODH) and formate-dehydrogenases (FDH) are the biological catalysts for reversible CO_2 reduction that contain mono- or multimetallic active sites composed of Earth-abundant metals ([NiFe]- and [MoSCu]-CODH and W- or Mo-FDH).[12−16] In addition to the CO_2-binding site provided by the metal active site, outer-sphere proton relays present in the enzyme often play an important role in catalysis. For instance, activation of CO_2 at the bimetallic active site of NiFe-CODH is facilitated by the stabilization of the bridged η^2-

Received: November 4, 2016
Published: February 16, 2017

DOI: 10.1021/jacs.6b11474
J. Am. Chem. Soc. 2017, 139, 3685−3696

Scheme 1. Synthesis of Cobalt-Diphosphine Complexes

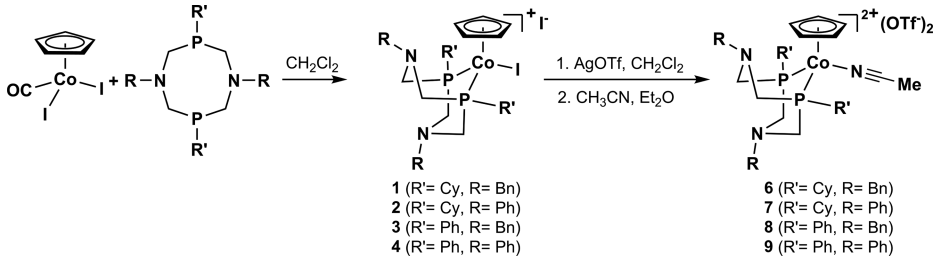

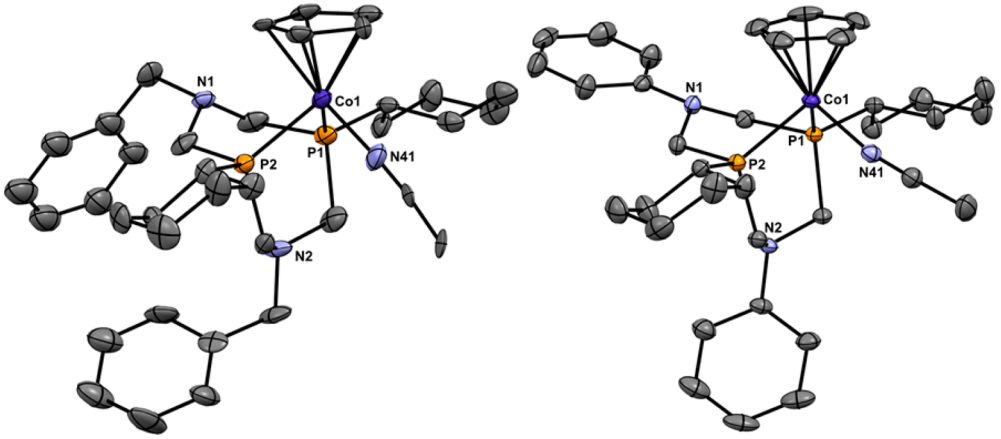

Figure 1. ORTEP diagrams of cations in **6** (left) and **7** (left) with ellipsoids shown at 50% probability. Hydrogen atoms are omitted for clarity.

CO_2-κ^2C_{Ni},O_{Fe} adduct through hydrogen-bonding interactions with closely spaced histidine and lysine residues. In a similar fashion, a pendant amine present in the diiron active site of [FeFe]-hydrogenases (H-cluster) has been shown to facilitate hydrogen evolution by shuttling protons to and from the iron centers.[17,18] Inspired by the influence of higher coordination sphere interactions on enzyme activity, many synthetic molecular catalysts have been reported as functional models of the enzymes. DuBois and co-workers at the Pacific Northwest National Laboratory have developed nickel-diphosphine electrocatalysts for hydrogen evolution and oxidation that feature proton relays in the second coordination sphere. The high activity of these complexes originates from the cooperative interaction of H_2 with both the nickel center and the multiple pendant amine groups in the secondary coordination sphere.[19−23] Similar nickel complexes have also been shown to catalyze electro-oxidation of formate, in which the pendant amines of P_2N_2 ligand act as bases and abstract protons from the Ni-bound formate.[24] The introduction of pendant proton relays also proved instrumental for the design of efficient molecular catalysts for CO_2 reduction. Nickel cyclam is a well-known CO_2-reducing compound that putatively uses an intramolecular H-bond to stabilize catalytic intermediate during CO production.[25,26] Savéant and co-workers have demonstrated that the CO_2-to-CO reduction performance of iron-tetraphenylporphyrin catalysts can be enhanced by increasing the local proton concentration via introduction of phenolic groups in the ortho positions of the phenyl rings.[27,28] More recently, Chapovetsky et al. have reported a cobalt-aminopyridine-based electrocatalyst for CO_2-to-CO reduction which contains outer-sphere secondary amines.[29] Other designs of catalysts containing pendant proton relays include Ir, Rh, and Fe complexes for hydrogenation of CO_2,[9,30−33] dehydrogenation of formic acid and methanol,[9,34,35] and reduction of O_2.[36−38]

Building on a similar design principle, we report here a new family of cobalt CO_2-reduction catalysts, $[CpCo(P^R_2N^{R'}_2)I]I$, where $P^R_2N^{R'}_2$ denotes a 1,5-diaza-3,7-diphosphacyclooctane ligand. Four different diphosphine ligands were used to prepare a series of cobalt complexes with the general formula $CpCo(P^R_2N^{R'}_2)I_2$: **1**, $P^R_2N^{R'}_2 = P^{Cy}_2N^{Bn}_2$;[39] **2**, $P^R_2N^{R'}_2 = P^{Cy}_2N^{Ph}_2$;[40] **3**, $P^R_2N^{R'}_2 = P^{Ph}_2N^{Bn}_2$;[41] **4**, $P^R_2N^{R'}_2 = P^{Ph}_2N^{Ph}_2$,[42] where Cy and Ph denote cyclohexyl and phenyl groups, respectively. These compounds exhibit excellent efficiency in terms of both catalytic rate and low overpotential requirement for reducing CO_2 to formic acid. Importantly, the process is highly selective, with little hydrogen and CO produced. These performances rank this series of catalysts among the most promising Earth-abundant molecular catalyst for CO_2-to-formic acid conversion.

RESULTS AND DISCUSSION

Synthesis and Characterization of Complexes. The cobalt complexes $[CpCo(P^R_2N^{R'}_2)I]I$ (**1**−**4**) were prepared by adding 1 equiv of ligand to a solution of $CpCo(CO)I_2$ in dichloromethane at room temperature (Scheme 1). These complexes were isolated as dark brown air-stable solids in excellent yields (75−88%). To evaluate the influence of the pendant amine groups, 1,3-bis(diphenylphosphino)propane (dppp) was used as the ligand to prepare an analogous cobalt compound ($[CpCo(dppp)I]I$, **5**) that did not contain amines in the outer coordination sphere. The complexes were characterized by ^1H and ^{31}P NMR, mass spectrometry, and optical spectroscopy. Several unsuccessful attempts to crystallize the iodo complexes, $[CpCo(P^R_2N^{R'}_2)I]^+$, prompted us to

DOI: 10.1021/jacs.6b11474
J. Am. Chem. Soc. 2017, 139, 3685−3696

remove both coordinated and non-coordinated iodide ions using silver triflate and generate the $[CpCo(P^R_2N^{R'}_2)(CH_3CN)](TfO)_2$ compounds (**6**, $P^R_2N^{R'}_2$ = $P^{Cy}_2N^{Bn}_2$; **7**, $P^R_2N^{R'}_2$ = $P^{Cy}_2N^{Ph}_2$; **8**, $P^R_2N^{R'}_2$ = $P^{Ph}_2N^{Bn}_2$; **9**, $P^R_2N^{R'}_2$ = $P^{Ph}_2N^{Ph}_2$) (Scheme 1). Bright red crystals of these triflate derivatives were obtained by slow diffusion of diethyl ether into concentrated acetonitrile (**6**–**8**) or dichloromethane (**9′**, see below) solutions of the complexes. X-ray crystal structures of **6** and **7** are shown in Figure 1, and the structures of **8** and **9′** are given in the Supporting Information (Figure S1). Molecular geometries of all four complexes are similar to the cobalt center adopting a three-legged piano-stool geometry expected for half-sandwich complexes of this type: the Cp ring binds in an η^5-manner and the Co-coordinated $P^R_2N^{R'}_2$ ligands form two six-membered rings, one of which is in a chair conformation and the other in a boat confirmation. An acetonitrile molecule occupies the third coordination site, except in the structure of **9′**, crystallized from **9** in CH_2Cl_2, which contains a triflate anion, instead of acetonitrile, coordinated to the cobalt center (Figure S1). With the notable exception of the positioning of the N and P substituents in the ligands, the four structures are very similar, with quasi-superimposable $[CoP_2((CH_2)_2N)_2]$ cores (Figure S2).

1–**4** are soluble in common organic solvents, such as dichloromethane, acetonitrile, and dimethylformamide (DMF), yielding brown-yellow solutions that are stable in air. They were further characterized by UV–vis spectroscopy, and their optical spectra in DMF (Figure S3) consist of three absorption maxima at λ = 370–390, 438, and 550–560 nm. The molar extinction coefficient values for the absorption bands at 370–390 and 438 nm ($\varepsilon_{370-390\ nm}$ = 1870–2670 M^{-1} cm^{-1}, and $\varepsilon_{438\ nm}$ = 1930–2750 M^{-1} cm^{-1}, respectively) are considerably larger than that for the absorption band at 550–560 nm ($\varepsilon_{370-390\ nm}$ = 500–550 M^{-1} cm^{-1}).

Electrochemical Characterization. Electrochemical properties of the complexes were investigated by cyclic voltammetry (CV) at a glassy carbon electrode in DMF (0.1 M NBu_4BF_4 as supporting electrolyte) under an atmosphere of argon (commercially available non-anhydrous DMF was used which contains ~0.2% water). As shown in Figure 2, the voltammograms of **1**–**4** display two one-electron electrochemical features in the −0.85 to −1.35 V vs $Fc^{+/0}$ range (unless otherwise mentioned, all potentials are referenced against the $Fc^{+/0}$ redox couple). In analogy to a previous report by Bullock and coworkers, these two couples can be assigned metal-centered $Co^{III/II}$ and $Co^{II/I}$ redox processes.[43] The half-wave potentials ($(E_{pa} + E_{pc})/2$) of each redox couple are listed in Table 1. The

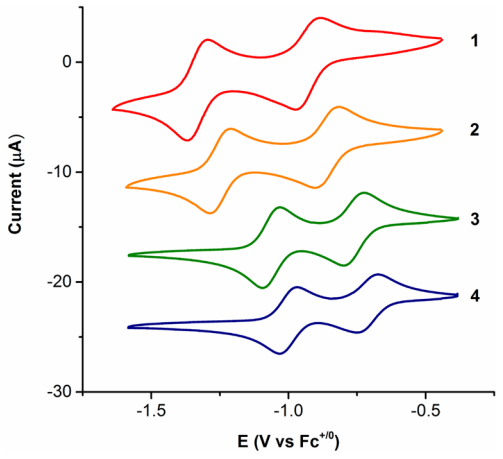

Figure 2. Cyclic voltammograms of **1** (red, 0.5 mM), **2** (orange, 0.5 mM), **3** (green, 0.6 mM), and **4** (blue, 0.6 mM) under Ar (ν = 0.1 V s^{-1} in DMF, 0.1 M NBu_4BF_4, glassy carbon electrode). The *Y*-axis is offset for clarity.

Table 1. Electrochemical Characterization of the Cobalt Complexes 1–4 in DMF (0.1 M NBu_4BF_4)

	$(E_{pa} + E_{pc})/2$, V (ΔE_p, mV)[a]	
complex	$Co^{III/II}$	$Co^{II/I}$
1	−0.97 (90)	−1.31 (64)
2	−0.90 (80)	−1.23 (64)
3	−0.88 (68)	−1.18 (64)
4	−0.86 (76)	−1.14 (62)
5	−0.75 (83)	−1.04 (60)

[a]Peak-to-peak separation between the cathodic and the anodic waves determined at 100 mV/s (under same conditions, $\Delta E_p(Fc^+/Fc)$ = 75 mV).

cathodic and anodic peak currents (i_p) for **1**–**4** vary linearly with the square root of the scan rate ($\nu^{1/2}$) from 0.05 to 0.25 V s^{-1} under Ar, consistent with diffusion-controlled processes as described by the Randles–Sevcik equation (Figure S4). Diffusion coefficients (D) in the range (1.5–3.6) × 10^{-6} cm^2 s^{-1} were calculated for **1**–**4** (Table S1). The peak-to-peak separation is consistent with reversible processes (ΔE_p = 62–80 mV, Table 1) for each redox couple, except the $Co^{III/II}$ process for **1** which appears quasi-reversible. The ratios of cathodic and anodic peak currents were close to unity, consistent with the chemical reversibility of those redox couples. The latter suggests that dissolution of the complexes is likely associated with the loss of the iodide ligand, resulting in the formation of $[CpCo(P^R_2N^{R'}_2)]^{2+}$cations in solution. This is further supported by the similar electrochemical behaviors of the iodo compounds (**1**–**4**) and their triflate analogues (**6**–**9**) (Figures S5 and S6). The $Co^{III/II}$ and $Co^{II/I}$ couples shift to more positive potentials as the phosphine groups of $P^R_2N^{R'}_2$ ligand become less electron donating and the amines become less basic. For instance, changing the ligand from $P^{Cy}_2N^{Bn}_2$ to $P^{Ph}_2N^{Bn}_2$ led to positive shifts of 90 and 130 mV for the $Co^{III/II}$ and $Co^{II/I}$ couples, respectively (Table 1). Similarly, potentials are shifted positively by 60 mV ($Co^{III/II}$) and 70 mV ($Co^{II/I}$) from $[CpCo(P^{Cy}_2N^{Bn}_2)]^{2+}$ to $[CpCo(P^{Cy}_2N^{Ph}_2)]^{2+}$. The $Co^{III/II}$ and $Co^{II/I}$ couples for **5**, the complex without any pendant amines, appear at less negative potentials compared to **1**–**4** (Table 1). These results suggest that the pendant amine groups, although not directly coordinated to the cobalt center, have a significant influence on its electronic properties.

Electrochemical CO_2 Reduction. Complexes **1**–**4** were evaluated as catalysts for electrochemical CO_2 reduction. The DMF electrolytic solution was saturated with CO_2 gas (~0.20 M) in the presence of various amounts of water.[44] Importantly, hydration of CO_2 forms H_2CO_3, which act as the proton source with pK_a = 7.37 in DMF.[27] Cyclic voltammograms of **1**, **2**, and **3**, recorded under CO_2 in DMF, displayed cathodic current enhancement (Figures 3 and S7). The mid-wave potential of this process was found at −2.08, −2.00, and −1.93 V for **1**, **2**, and **3**, respectively. In contrast, the cyclic voltammogram of **4** was unchanged upon addition of CO_2 (1 atm) in DMF.

DOI: 10.1021/jacs.6b11474
J. Am. Chem. Soc. 2017, 139, 3685–3696

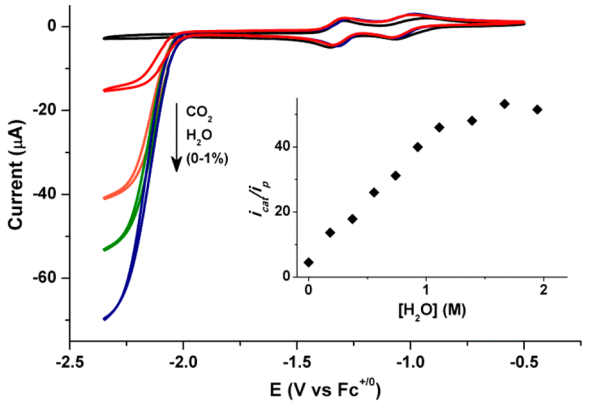

Figure 3. Cyclic voltammograms of **1** (1 mM) under Ar saturation (black), under CO_2 saturation (red), and under CO_2 saturation in the presence of increasing amount of water; orange, 0.33% (v/v); green, 0.67% (v/v); and blue, 1% (v/v). The inset shows the influence of the concentration of water on the catalytic current. Voltammograms were recorded at 0.1 V s^{-1} in 0.1 M NBu_4BF_4 in DMF using a glassy carbon electrode.

Incremental addition of water to CO_2-saturated DMF solutions of **1**−**3** resulted in increased current densities, before reaching a maximum value and then leveling off with larger concentrations of water (>1.5, 3, and 3.5 M for **1**, **2**, and **3**, respectively). In a control experiment, addition of saturated aqueous CO_2 solution to an Ar-saturated DMF solution of **1** led to current enhancement at the same potential as of CO_2 (see Figure S29). In the case of **4**, a weak cathodic wave was observed with mid-wave potential at ca. −1.88 V, upon addition of water (Figure S8). Importantly, no current enhancement was observed in DMF/water mixtures in the absence of catalyst or CO_2 (see Supporting Information). Notably, very small catalytic current was observed when **5** was employed as the catalyst in CO_2-saturated DMF/water mixtures (Figure S9), strongly suggesting a critical role of the pendant amine groups during electrocatalysis.

Controlled-Potential Electrolysis Experiments. The observed current enhancement corresponds to the electrocatalytic reduction of CO_2 to formic acid, as verified by controlled-potential electrolysis (CPE) carried out at mercury-pool working electrodes (surface area = 1.77 cm^2) with 0.5 mM catalyst (**1**−**4**) in CO_2-saturated DMF/H_2O. In general, the CPE experiments were conducted for 1 h or up to complete catalyst deactivation. During the course of electrolysis, the current density was initially quite stable at ∼0.6−1.8 mA cm^{-2} and then slowly decayed until it reached the level of background current. In general, the initial period of stability was shorter for higher current densities at more negative potentials, suggesting catalyst decomposition is faster under more severe conditions. A change of color of the solution from bright brown-yellow to colorless is observed at the end of the CPE experiment. The electrocatalytic current could be restored by addition of fresh catalyst which confirmed that catalyst degradation is the limiting factor (Figure S10). To study the effect of applied potential on product distribution and rate, different potentials were tested for **1**−**3**, in the range −2.00 to −2.25 V vs $Fc^{+/0}$ (Figure S11). In general, electrolysis at higher overpotentials led to faster catalysis, however over shorter duration (Figure S11A). The electrolysis results are summarized in Table 2. Analyses of post electrolysis solutions by ionic chromatography revealed the generation of large amounts of formic acid with excellent Faradaic yields (FY = 86−100%) only in the case of **1**−**3** (Table 2). Small amounts of CO (FY = 0−1%) and H_2 (FY = 2−11%) were also detected as the gaseous products by gas chromatography. Formic acid, CO, and H_2 were not detected when the electrolysis of a CO_2-saturated DMF/H_2O mixture was carried out in the absence of catalyst. Total catalytic turnover numbers for formic acid (TON_{HCOOH}) were determined from the amount of formic acid produced after 1 h electrolysis. The Faradaic yields for formic acid production remained unaffected, but the TON_{HCOOH} increased upon applying more negative potentials (Table 2, entries 1−5 for **1**, entries 6−9 for **2**, Figure S12). Catalyst **1** displayed best activity with TON_{HCOOH} = 23 and 15 in the presence of 1.1 and

Table 2. Conditions for the Controlled Potential Electrolyses and Product Analyses

				faradaic yield, %					
entry	catalyst (0.5 mM)	E, V/$Fc^{+/0}$	[H_2O], M	HCOOH (±8)	CO (±1)	H_2 (±5)	TON_{HCOOH} [a] (1 h) (±20%)	TOF^{CPE}_{HCOOH} [b], s^{-1} (±20%)	η (applied)[c], V
1	**1**	−2.10	1.1	92	<1	5	8	70	0.65
2	**1**	−2.15	1.1	88	<1	3	10	150	0.70
3	**1**	−2.20	1.1	86	<1	4	12	250	0.75
4	**1**	−2.25	1.1	98	<1	5	23	650	0.80
5	**1**	−2.25	0.56	92	<1	10	15	–	0.80
6	**2**	−2.05	1.1	94	1	3	5	60	0.6
7	**2**	−2.10	1.1	91	1	3	7	100	0.65
8	**2**	−2.15	1.1	99	<1	3	9	180	0.7
9	**2**	−2.20	1.1	98	<1	4	9	180	0.75
10	**2**	−2.20	2.8	95	<1	3	8	–	0.75
11	**3**	−2.00	1.1	88	<1	8	2	20	0.55
12	**3**	−2.05	1.1	86	<1	6	4	40	0.60
13	**3**	−2.15	2.8	92	<1	11	7	–	0.75
14	**4**	−2.1	5.6	38	1	67	1.5	–	0.65
15	**1**	−2.15	20 mM $[Et_3NH]^+$ (0 M H_2O)	48	<1	52	11	–	0.70

[a] TON_{HCOOH} is the total turnover number for formic acid after 1 h. [b] TOF^{CPE}_{HCOOH} is the turnover frequency for formic acid generation, derived from electrolyses data using the equations described by Savéant et al. (see Supporting Information).[3,27,28,53] [c] Overpotentials are calculated using E^0(CO_2/HCOOH) = −1.45 V vs $Fc^{+/0}$ (see Supporting Information).

DOI: 10.1021/jacs.6b11474
J. Am. Chem. Soc. 2017, 139, 3685−3696

0.56 M water, respectively, after electrolysis at −2.25 V for 1 h (Table 2, entries 4 and 5). Only **4** displayed poor catalytic performance in terms of both product selectivity (FY_{HCOOH} = 38%) and total catalytic TON (Table 2, entry 14), in line with the weak catalytic wave observed in its cyclic voltammograms. Notably, electrolysis with **4** was carried out in the presence of large excess of water (5.6 M) as its voltammograms showed very little electrocatalysis at low water concentration. Consequently, a considerably higher amount of H_2 (FY_{H_2} = 67%) was produced during the electrolysis with **4**. Catalytic selectivity of **1** was further tested by performing CV and CPE in the presence of CO_2 and $Et_3NH^+Cl^-$ (Figure S13). Formic acid and hydrogen were produced by CPE with 48(±5)% and 52(±5)% Faradaic efficiencies, respectively, corresponding to ∼11 turnovers for formic acid (TON_{HCOOH}) and ∼12 turnovers for hydrogen (TON_{H_2}) after 1 h (Table 2, entry 15).

Notably, similar values for TON_{HCOOH} was obtained when glassy-carbon or graphite rod was used as working electrodes, but FY_{HCOOH} was significantly lower (20−50%) because a larger amount of H_2 was produced (FY_{H_2} = 45−60%) (Table S2 and Figure S14). In the absence of any catalyst, a small amount of formic acid was produced by direct reduction of CO_2 at the graphite electrode. Deposition of cobalt nanoparticles on the carbon electrode through decomposition of the molecular complexes may account for the color change observed in the course of long-term electrolysis, and it is well known that such deposits catalyze hydrogen evolution, in addition to H_2 evolution occurring directly at the surface of the carbon electrode.[45,46] On the other hand, use of mercury electrode ensured that metallic cobalt nanoparticles amalgamated and, consequently, proton reduction was suppressed.

Determination of Kinetic Data and Benchmarking of Catalytic Performances. The catalytic cyclic voltammograms of **1**−**4** were further analyzed to probe the kinetics of the electrocatalytic CO_2 reduction. For all complexes, catalytic cyclic voltammograms show typical S-shaped response. The catalytic plateau current (i_{cat}) varies linearly with the catalyst concentration, consistent with a mechanism for CO_2 reduction that is first-order in catalyst (Figure S15). Electrocatalytic reactions are also first-order in CO_2, which is evidenced by the linear dependence of normalized peak catalytic current (i_{cat}/i_p; i_p is determined as the $Co^{II/I}$ peak current) on the square root of [CO_2] as the CO_2 partial pressure was varied between 0.2 and 1 atm in N_2/CO_2 gas mixtures (Figure S16). No saturation of the catalytic current with increasing CO_2 concentration was detected, indicating that CO_2 is involved in the rate-limiting step. Additionally, i_{cat} reaches a limiting value (Figures 3 and S7) at high water concentration (>1.5, 3, and 3.5 M for **1**, **2**, and **3**, respectively), suggesting saturation kinetics in which concentration of water is sufficiently high that it is not depleted during the course of the experiment. KIE analysis was carried out within a concentration range of water suitable to get a reaction order of 2 in protons, i.e., linear dependence of i_{cat}/i_p on water concentration (0−1.5 M). Normal H/D kinetic isotope effects (KIEs) of 5.0 (±0.4), 10.4 (±0.7), and 5.7 (±0.6) were found for **1**, **2**, and **3**, respectively (Figures 4 and S17). The catalytic current plateaus in catalytic voltammograms are scan rate-independent for each complex (Figure S18), indicating catalysis in the pure kinetic regime.[47] Under such conditions, the normalized peak catalytic current (i_{cat}/i_p) is related to the maximum turnover frequency (TOF_{max}) of the

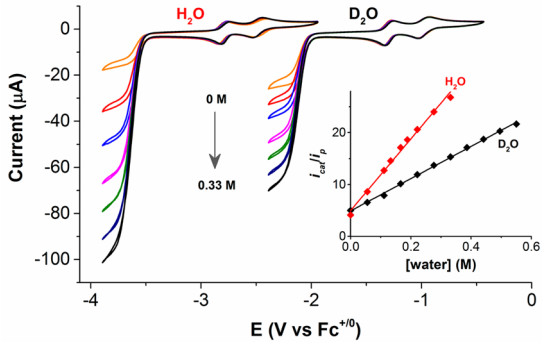

Figure 4. KIEs demonstrated by cyclic voltammograms of **1** (0.6 mM) recorded in CO_2-saturated DMF in the presence of varying amount Brönsted acid (H_2O or D_2O). The *x*-axis is offset by −1.5 V for clarity. Linear dependence of i_{cat}/i_p on concentration of water (analogous to plotting $k_{CO_2}^{1/2}$ vs [water]) is shown in the inset. Cyclic voltammograms were recorded in DMF (0.1 M NBu_4BF_4) using a glassy carbon electrode at 0.1 V s^{-1}.

electrocatalysis by eq 1,[27,48] accounting for a simplified two-electron mechanism with a single rate-determining step:

$$i_{cat}/i_p = 4.484\sqrt{\frac{RT}{F}}\sqrt{TOF_{max}}\nu^{-1/2} \quad (1)$$

TOF_{max} values for **1**−**4** under various water concentrations were calculated (Figures S19 and S20, and more details in the Supporting Information) and summarized in Table 3. Catalyst **1** operates at highest rate with TOF_{max} values estimated to be ∼1000 s^{-1} at >1.5 M water. Catalyst **4** showed the lowest activity and the estimated TOF_{max} was below 1 s^{-1} in up to 4 M water/DMF mixtures.[49] At any fixed water concentration, a clear trend for the rate of electrocatalysis rate was observed: **1** ≫ **2** > **3** ≫ **4**. It follows the evolution of the overpotential value for CO_2 to formic acid conversion at which the plateau value is reached: $E_{cat}^{pl}(\mathbf{1}) < E_{cat}^{pl}(\mathbf{2}) < E_{cat}^{pl}(\mathbf{3}) < E_{cat}^{pl}(\mathbf{4})$. This interplay between TOF and applied potential is better illustrated in the catalytic Tafel plots shown in Figure 5. To build such plots, the standard reduction potential of the CO_2/HCOOH couple in DMF/H_2O solutions ($E^0_{CO_2/HCOOH(DMF)}$ = −1.45 V)[50−52] was subtracted from the applied potential to give the overpotentials (η).

Turnover frequencies (TOF^{CPE}_{HCOOH}) could also be obtained from the preparative-scale electrolyses at different operating overpotential, using the equations reported by Savéant and co-workers (see the Supporting Information for details).[3,27,28,48,53] The values are listed in Table 2. It should be noted that the ohmic drop is much more important in the case of CPE experiments relative to CV measurements. It has a direct effect on the current measured, and this explains why TOF_{max} and TOF^{CPE}_{HCOOH} values differ. We nevertheless note that they have the same order of magnitude. The TOF^{CPE}_{HCOOH} value for **1**, derived from the electrolysis data, is 650 s^{-1} at 1.1 M water, which corresponds to generation of formic acid with a catalytic TON = 780 000 within 20 min (TON = $TOF^{CPE}_{HCOOH} \times t$, where t = 1200 s). TOF_{CPE} values determined for **1**−**3** are presented as crosses within the same catalytic Tafel plot. As shown in Figure 5, they satisfactorily match the log TOF−η plots derived from the CV measurements. The log TOF−η plots generated from CV data in DMF/water (1.1 M) mixtures provide a direct comparison of all four cobalt catalysts reported here. These catalysts are benchmarked against an iridium-hydride electro-

DOI: 10.1021/jacs.6b11474
J. Am. Chem. Soc. 2017, 139, 3685−3696

Table 3. Turnover Frequencies from CV Experiments (TOF_{max}^{CV}) for the Cobalt Complexes 1−4 in the Presence of Different Concentrations of Water

	TOF_{max}^{CV} or k_{cat}^{CV}, s^{-1}			
	1	2	3	4
$[H_2O]$, M	η = 0.60−0.72 V[a]	η = 0.55−0.61 V[a]	η = 0.50−0.54 V[a]	η = 0.36−0.44 V[a]
0	1(1)	<1	<1	<1
0.56	2(0.4) × 10^2	2(0.5) × 10^1	1(1)	<1
1.11	4(0.5) × 10^2	3(0.2) × 10^1	4(1)	<1
1.67	1(0.1) × 10^3	7(0.5) × 10^1	1(0.2) × 10^1	<1
2.23	~10^3 (0.72)[b]	8(0.5) × 10^1	2(0.2) × 10^1	<1
3.34	~10^3 (0.72)[b]	3(0.2) × 10^2	7(0.5) × 10^1	<1

[a] $\eta = [(-1.45) - E_{1/2}^{cat}]$ (V); $E_{1/2}^{cat}$ became more negative at higher water concentrations, leading to larger overpotential. [b] At these water concentrations, the plateau shape of the catalytic wave for **1** was lost, and so the measure is less precise.

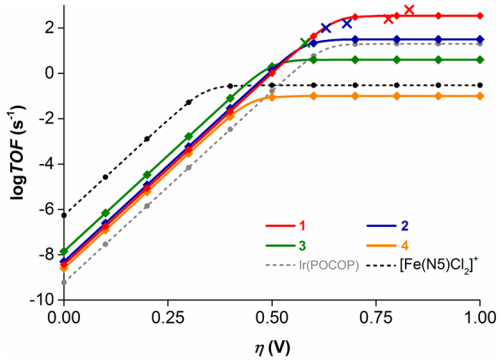

Figure 5. Benchmarking of the catalysts based on catalytic Tafel plots derived from the cyclic voltammograms in 1.1 M water/DMF mixtures. The crosses indicate the TOF values obtained from chronoamperometric data from the initial 20 min of electrolyses in 1.1 M water/DMF mixtures. Plots for the Ir and Fe catalysts were derived from the data reported by Kang et al.[54] and Taheri et al.,[56] respectively.

catalyst (Ir-PCP; PCP denotes a pincer ligand), previously reported by Meyer and co-workers, that selectively reduces CO_2 to formic acid.[54,55] The most active cobalt catalysts in our series of complexes (**1** and **2**) display faster rate and greater TOF_{max} relative to Ir-PCP. Importantly, the overpotential required to achieve maximum TOF for **1** is similar to that for Ir-PCP. The overpotential requirement for **2** is ~150 mV lower than that for Ir-PCP, while their TOF_{max} values are similar. We also benchmarked the performances of **1**−**4** against that of $[Fe(N5)Cl_2]^{2+}$ (N5 = (2,13-dimethyl-3,6,9,12,18-pentaazabicyclo[12.3.1]octadeca-1(18),2,12,14,16-pentaene), which displays good selectivity for CO_2-to-formic acid conversion with TOF values more than 3 orders of magnitude lower than that for **1**, and an overpotential requirement of only ~100 mV lower.[50] Berben and co-workers described another iron-based catalyst, $[Fe_4N(CO)_{12}]^-$, which is selective to formic acid formation and operates at a more positive potential (−1.6 V vs Fc^+/Fc) in CH_3CN/H_2O (95:5 v/v), corresponding to an overpotential of ~200 mV, however, with a slower kinetics (TOF_{CV} = 10 s^{-1}) compared to the cobalt catalysts presented herein.[6,56−58]

Density Functional Theory (DFT) Calculations and Mechanistic Considerations. Scheme 2 shows a proposed mechanism for electrocatalytic CO_2 reduction that is consistent with the electrochemical studies and is supported by DFT calculations performed on two different models of the acetonitrile derivative of **1** (real system = $\mathbf{1}^{MeCN}$-Real = $[CpCo(P^{Cy}_2N^{Bn}_2)(MeCN)]^{2+}$; model system = $\mathbf{1}^{MeCN}$-Model = $[CpCo(P^{Me}_2N^{Me}_2)L]^{2+}$) and the acetonitrile derivative of **5** ($\mathbf{5}^{MeCN}$ = $[CpCo(dppp)(MeCN)]^{2+}$) shown in Figure 6. The optimized structures of key catalytic intermediates of $\mathbf{1}^{MeCN}$-Model and the transition state for the CO_2 insertion reaction ($\mathbf{1}^{MeCN}$-Real, $\mathbf{1}^{MeCN}$-Model and $\mathbf{5}^{MeCN}$) are shown in Figures S21 and S22. Indeed, experiments have shown that a Co^{II}-H intermediate generated near −2.0 V vs Fc^+/Fc is competent for catalytic H_2 evolution (see Figures S23 and S24), in line with previous reports on comparable complexes.[43,59,60] Upon addition of CO_2, enhanced currents are also observed at this potential. This suggests that the same Co^{II}-H intermediate (**V**) is involved in both H_2 evolution and CO_2 reduction. According to DFT calculations, **V** can be produced from the initial Co^{III} species **I** through three different pathways, as shown in Scheme 2 and detailed below. After two successive electron transfers, a Co^I species (**III**) is generated. This species is then protonated and further reduced to form a cobalt(II)-hydride (Co^{II}-H) species (**V**, Scheme 2). DFT calculations suggest a concerted proton-coupled electron-transfer (PCET) process, as our calculation for the redox potential of a Co^{III}-H/Co^{II}-H couple (−2.5 V vs Fc^+/Fc), that would involve a sequential pathway (Scheme S2, top panel), was systematically more negative than the experimental potential (−2.1 V vs Fc^+/Fc) at which both H_2-evolution and CO_2-reduction reactions are catalyzed. Instead, the computed redox potential (−2.0 V vs Fc^+/Fc) of the (Co^I, R_3NH^+)/(Co^{II}-H, R_3N) couple (R_3N denotes a pendant amine) was found in line with the experimental observation. (Note that H_2CO_3 has a pK_a value similar to that of Et_3NH^+ in DMF.) DFT calculations indicated that protonation of the pendant amine in either the Co^{II} or Co^I states (Scheme S2, middle and bottom panels) allows two other pathways through intermediates **III′** and **IV**, respectively, through intramolecular proton transfer to cobalt concerted with reduction of the metal center. While no Co^{II}-H species with similar coordination spheres have been isolated so far, they have been evidenced in studies on Co^{III}-H derivatives by Kölle and Paul[59] and by DuBois, Bullock, and co-workers.[43] The Co^{II}-H species **V** then reacts with CO_2, generating **VI**. Internal hydride transfer from cobalt to CO_2 then yields **VII**.[61] The extrusion of formic acid from **VII** regenerates the Co^{II} species **II** and completes the catalytic cycle. The Co^{III} complexes are air-stable and easy to handle. They are, however, better described as precatalysts for CO_2 reduction, as they require an additional electron to generate the catalytically competent Co^{II} species.[62,63]

DOI: 10.1021/jacs.6b11474
J. Am. Chem. Soc. 2017, 139, 3685−3696

Scheme 2. Postulated Mechanism for Electrocatalytic CO_2 Reduction[a]

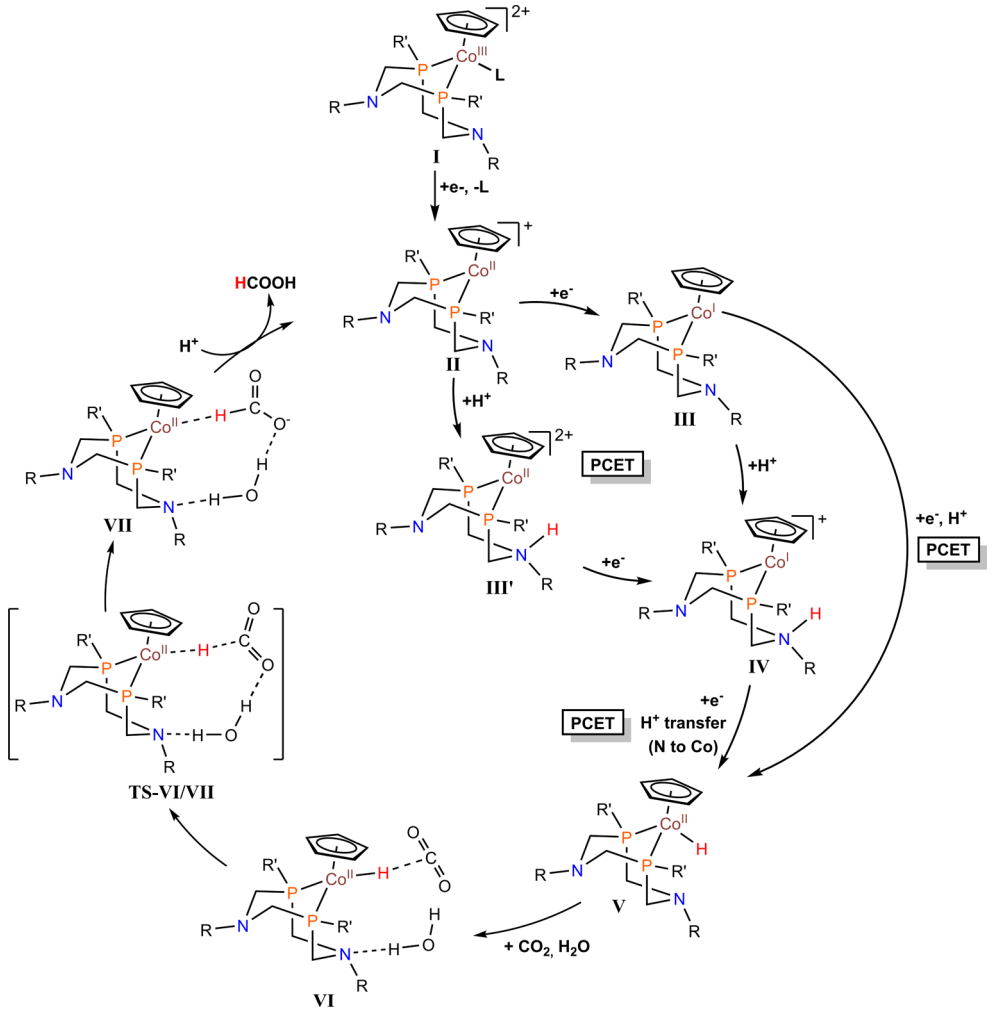

[a]See Figure S22 for DFT structures of intermediates and transition state calculated for the $\mathbf{1}^{MeCN}$-Real model.

DFT calculations indicate that addition of water to the system is advantageous, thanks to the formation of intramolecular hydrogen bonding involving the bound CO_2/formate molecules and one pendant amine residue. First, hydride transfer (Scheme 2, **VI** to **VII**) is thermodynamically more favorable when the amines are present (Figure 6) because the $[Co\cdots HCO_2^-]$ species (**VII**, Scheme 2) is stabilized by H-bonding with the amine-bound water molecule. Second, calculated barriers are relatively small, irrespective of the model employed to describe the transfer of hydrogen to CO_2 (Figure 6). The prominent role of amine residues is further supported by DFT calculation on $\mathbf{5}^{MeCN}$ that lacks such pendant amine groups. In that case, significantly higher activation energy is observed for the CO_2 insertion step (Figure 6 and Table S3).

Such a mechanistic scheme provides a rationale for the faster electrocatalytic rates observed for **1** and **3** with the more basic benzylic amine groups compared to the corresponding complexes **2** and **4** containing less basic aniline residues. In organic solvents, free benzylamine is a stronger base than aniline ($pK_a^{CH_3CN}$ = 16.91 and 10.62 for $BnNH_3^+$ and $PhNH_3^+$, respectively),[64,65] and a similar trend would be expected for the pendant bases in **1**–**4**. The stronger benzylamine base (complexes **1** and **3**) would provide greater stabilization to the transition state during hydride transfer (**TS-VI/VII**, Figure 6) through H-bonding.

The mechanism shown in Scheme 2 also agrees with the experimentally determined first-order electrocatalytic rate in the catalyst and CO_2 concentration, under the assumption that the intermediate CO_2 adduct exists in rapid equilibrium with the Co^{II}-H species and CO_2. This type of kinetics is at variance with that previously proposed by Ahn et al. for CO_2 electroreduction by pincer iridium catalysts involving formate release as the rate-determining step.[30] In the proposed mechanism, CO_2 does not interact directly with the metal center (C-coordination of CO_2 usually leads to CO formation),[66] and instead, the whole catalyst acts as a hydride-transfer reagent. A similar mechanism, based on computation, has been recently proposed for putative CO_2 hydrogenation by an iron catalyst containing a similar diphosphine ligand with pendant amine residues.[67] Such a pathway is, however, at variance with that based on CO_2 insertion in a metal–hydride bond reported for other catalysts for CO_2 hydrogenation catalysts[31,68−70] or electrocatalysts for formic acid production.[30,55] In this mechanism, as well as in the reverse mechanism proposed for formate oxidation catalyzed by nickel bisdiphosphine complexes with similar pendant amine residues,[24,41,71] formate binds to the metal center through an oxygen atom, and formate

DOI: 10.1021/jacs.6b11474
J. Am. Chem. Soc. 2017, 139, 3685−3696

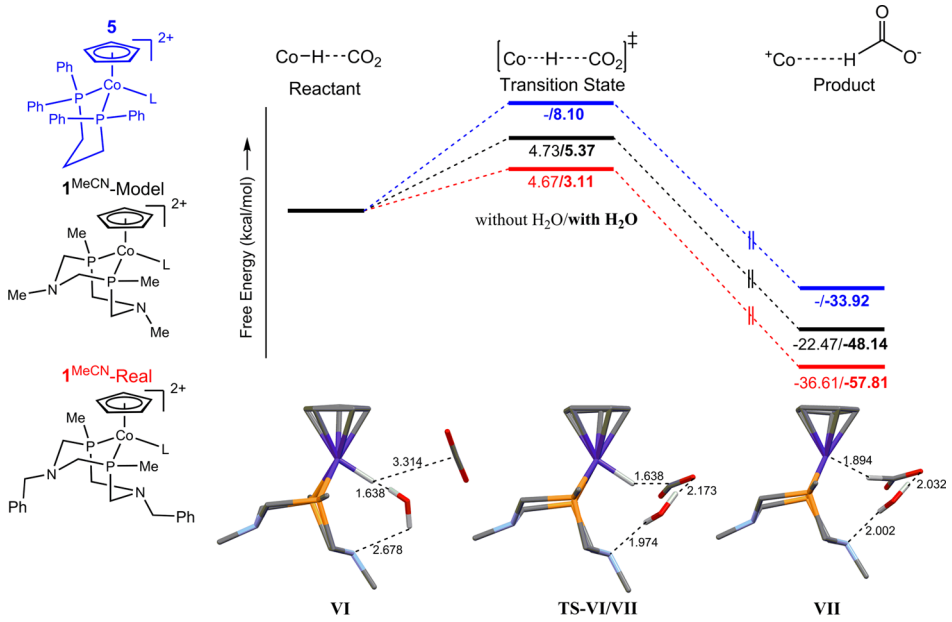

Figure 6. Free energy diagram for the CO_2-reduction step involving Co^{II}-hydride species in gas phase in the presence and absence of water. The relative free energies were calculated for $\mathbf{1}^{\mathbf{MeCN}}$ using two different systems: $[CpCo(P^{Cy}{}_2N^{Bn}{}_2)(MeCN)]^{2+}$ ($\mathbf{1}^{\mathbf{MeCN}}$-Real, red) and $[CpCo(P^{Me}{}_2N^{Me}{}_2)(MeCN)]^{2+}$ ($\mathbf{1}^{\mathbf{MeCN}}$-Model, black). The calculated relative free energies for $\mathbf{5}^{\mathbf{MeCN}}$ are shown in blue. The structures of hydride intermediate and transition state calculated using $\mathbf{1}^{\mathbf{MeCN}}$-Real system (gas phase) are shown in the bottom panel (phenyl and cyclohexyl groups are omitted for clarity). All distances and energies are in Å and kcal·mol^{-1} respectively.

release has sometimes been found as the rate-determining step.[30] Rather, the catalytic pathway proposed here resembles the mechanism followed by catalytic hydride donors based on dihydropyridine moieties,[72,73] in which hydride transfer can be assisted by hydrogen-bonded water molecules. It should also be noted that similar mechanism is operative for several stoichiometric CO_2-reducing organohydride reagents including hydrosilanes,[74] hydroboranes,[75,76] and ammonia boranes.[77] The fairly large (>5) H/D KIE values observed for these catalysts support hydride transfer from Co to CO_2, involving concomitant cleavage of Co−H and formation C−H bonds in the rate-determining step. For comparison, KIE values of ∼2 have been reported for CO-producing mechanisms, involving proton transfers only, catalyzed by rhenium and iron complexes.[78,79]

Another prominent feature is the excellent selectivity of the catalysts toward CO_2 over proton reduction. We used DFT to compute the activation barriers for CO_2 reduction and H_2 evolution from the Co^{II}-H intermediate in the absence and presence of water molecules. In line with experimental observations, additional DFT calculations suggested that the presence of water favors CO_2 reduction by stabilizing the Co^{II}-H by hydrogen bonding. It leads to an increase in the activation barrier for H_2 evolution to ∼10 kcal mol^{-1} which is considerably higher than the ∼3 kcal mol^{-1} barrier computed for CO_2 reduction (Figure 6). In the absence of water, the barriers for CO_2 reduction (Table S4) and H_2 evolution (Scheme S3) are ∼4.7 and ∼5.2 kcal mol^{-1}, respectively, thus in line with the lower selectivity experimentally observed when $[Et_3NH]^+$ is used as a proton source.

CONCLUSION

Most molecular CO_2-reducing catalysts produce CO. In addition to enzymes, there are few synthetic catalysts that generate formic acid,[30,50,54−58,80−90] and among them only two are selective and based on an Earth-abundant metal.[50,56,57] Nickel bis-diphosphine complexes bearing pendant amine groups, $[Ni(P^R{}_2N^{R'}{}_2)_2]^{2+}$, have been shown to catalyze the reverse reaction, i.e., formate oxidation, quite efficiently,[24,41,71] and this was related to the fact that the corresponding Ni^{II}-hydride species have lower hydridicities[91] than formic acid ($\Delta G^\circ_{H^-}$ = 44 kcal mol^{-1} in CH_3CN).[57] Such low hydridicities explain also why $[Ni(P^R{}_2N^{R'}{}_2)_2]^{2+}$ complexes require strong acids to evolve hydrogen in CH_3CN under electro-assisted conditions. By contrast, cyclopentadienyl diphosphine cobalt complexes have previously been reported as electrocatalysts for hydrogen evolution that involves reduction of an intermediate hydride, $CpCo^{III}$(diphosphine)-H.[43,59,60] The introduction of pendant amines proved beneficial for H_2 evolution catalysis although still with large overvoltage requirement. We reasoned that such a lower activity for proton reduction probably results in higher hydridicity for the intermediate $CpCo^{II}$(diphosphine)-H, making hydride transfer to CO_2 favorable. Actually, this class of cobalt-based molecular compounds proved as quite active precatalysts for electrochemical CO_2 reduction reported so far, with two particularly notable features: (1) their excellent selectivity for reduction of CO_2 to formic acid and (2) the ability to tune their activity via ligand design. Four different $P^R{}_2N^{R'}{}_2$ ligands with cyclohexyl or phenyl substituents on phosphorus (P^{Cy} or P^{Ph}) and benzyl or phenyl substituents on nitrogen (N^{Bn} or N^{Ph}) were indeed employed, and all complexes displayed catalytic activity toward electrochemical reduction of CO_2 to formic acid with excellent Faradaic efficiency (90 ± 10%) and good TON at moderate overpotentials (400−600 mV in DMF). Complex **1**, which contains the ligand with the most electron-donating phosphine and the most basic amine ($P^{Cy}{}_2N^{Bn}{}_2$), performs best among the series with a remarkable TOF (>1000 s^{-1}). Comparison of the catalytic activity of the cobalt complexes with $P^R{}_2N^{R'}{}_2$ ligands

DOI: 10.1021/jacs.6b11474
J. Am. Chem. Soc. 2017, 139, 3685−3696

(**1**−**4**) and that of the related complex **5**, which does not contain the pendant amines, clearly indicates that the nitrogen substituents of the $P^R{}_2N^R{}_2$ ligands play an important role in the catalytic activity for these complexes and suggest that more basic amines favor catalytic CO_2 reduction. Mechanistic studies indicated that such amine groups are not involved in direct proton transfer to CO_2 but rather in the stabilization of key intermediates through hydrogen bonding with water molecules during hydride transfer. Only three CO_2-reducing molecular electrocatalysts (one based on iridium and the other two based on iron) were known so far to selectively produce formic acid.[50,54,56,57] State-of-the-art benchmarking of performances clearly revealed that these new cobalt catalysts outcompete all of them in terms of maximum TOF, even if the $[Fe_4N(CO)_{12}]^-$ cluster reported by Berben and co-workers displays much lower overpotential requirement.[56] The highest overall TON_{HCOOH} of 23 (electrolysis at −2.2 V for 1 h) observed for **1** is comparable to those obtained for other three formate-producing electrocatalysts: Ir-PCP, TON ≈ 40 after 25 h electrolysis;[54] $[Fe(N5)Cl_2]^{2+}$, TON ≈ 3.6 after 3 h electrolysis;[50] $[Fe_4N(CO)_{12}]^-$, TON ≈ 15 ± 3 after 1 h electrolysis.[5] However, in contrast to Ir-PCP and $[Fe_4N(CO)_{12}]^-$, the cobalt catalysts are limited by their stability under prolonged electrolysis, as complete loss of activity is observed after 1 h. Still, the straightforward synthesis of such complexes, combined with the large possibility offered by diphosphine ligands in terms of ligand tuning and outer-sphere control,[92] holds promise for optimization of performances and the preparation of molecular-engineered electrode and photoelectrode materials.[93]

EXPERIMENTAL SECTION

Reagents and Materials. The ligands $P^{Cy}{}_2N^{Bn}{}_2$, $P^{Cy}{}_2N^{Ph}{}_2$, $P^{Ph}{}_2N^{Bn}{}_2$, and $P^{Ph}{}_2N^{Ph}{}_2$ were prepared according to reported procedures.[39−41,94] The precursor $CpCo(CO)I_2$ was synthesized by literature method.[95] All other reagents, including cyclopentadienylcobalt dicarbonyl ($CpCo(CO)_2$, 95%) and tetrabutylammonium tetrafluoroborate ($^nBu_4NBF_4$, 99%), are commercially available and were used as received. Acetonitrile, dichloromethane, diethyl ether, and tetrahydrofuran were dried and distilled using common techniques. All manipulations of phosphine-containing compounds were carried out under an atmosphere of purified argon in a glovebox or by standard Schlenk techniques.

General Procedure for the Synthesis of CpCo(diphosphine)-I_2 Compounds. The diphosphine ligand (0.2 mmol) was added to a black brown solution of $CpCo(CO)I_2$ (0.081 g, 0.2 mmol) in anhydrous CH_2Cl_2 (15 mL), and evolution of CO was observed immediately. After the solution was stirred for 4 h at room temperature, the volatiles were removed under reduced pressure. The residue was subjected to silica gel-column chromatography with 1% CH_3OH/CH_2Cl_2 to give the pure product as a dark brown solid.

*$CpCo(P^{Cy}{}_2N^{Bn}{}_2)I_2$ (**1**).* Yield 0.129 g (74%). ^1H NMR (300 MHz, $CDCl_3$) δ_{ppm}: 1.1−1.98 (m, 18H), 2.46−2.62 (m, 4H), 2.84 (m, 2H), 3.20 (m, 2H), 3.34 (m, 2H), 3.54 (s, 2H), 3.87 (m, 2H), 4.27 (s, 2H), 5.67 (s, 5H), 6.96 (m, 2H), 7.26−7.47 (m, 8H). ^{31}P NMR ($CDCl_3$): 41.6 (s) ppm. Analysis Calculated for $C_{35}H_{49}CoI_2N_2P_2$: C, 48.18; H, 5.66; N, 3.21. Found: C, 49.80; H, 5.97; N, 3.38. SIM-MS: 745.2 $[M - I]^+$. λ_{max}, nm (ε, M^{-1} cm^{-1}): 372 (1900), 438 (1900), 560 (400).

*$CpCo(P^{Cy}{}_2N^{Ph}{}_2)I_2$ (**2**).* Yield 0.120 g (70%). ^1H NMR (300 MHz, $CDCl_3$) δ_{ppm}: 1.2−1.9 (m, 10H), 1.90 (m, 8H) 2.20 (m, 2H), 2.68 (m, 2H), 3.43 (m, 2H), 4.04−4.28 (m, 6H), 3.56 (s, 2H), 3.91 (m, 2H), 4.29 (s, 2H), 5.85 (s, 5H), 6.97 (d, 2H), 7.06 (m, 2H), 7.35 (q, 4H), 7.55 (d, 2H). ^{31}P NMR ($CDCl_3$): 42.4 (s) ppm. Analysis Calculated for $C_{33}H_{45}CoI_2N_2P_2$: C, 46.94; H, 5.37; N, 3.32. Found: C, 47.60; H, 5.39; N, 3.32. SIM-MS: 717.2 $[M - I]^+$. λ_{max}, nm (ε, M^{-1} cm^{-1}): 385 (2400), 438 (2800), 554 (500).

*$CpCo(P^{Ph}{}_2N^{Bn}{}_2)I_2$ (**3**).* Yield 0.130 g (76%). ^1H NMR (300 MHz, $CDCl_3$) δ_{ppm}: 3.25 (m, 4H), 3.66 (s, 2H), 3.88 (d, 2H), 4.27 (m, 2H), 4.64 (s, 2H), 5.36 (s, 5H), 7.03 (m, 2H), 7.26 (2H, masked by $CDCl_3$ peak), 7.41 (q, 4H) 7.56 (s, 6H), 7.65 (d, 2H), 8.03 (br, 4H). ^{31}P NMR ($CDCl_3$): 31.7 (s) ppm. Analysis Calculated for $C_{35}H_{37}CoI_2N_2P_2$: C, 48.86; H, 4.33; N, 3.26. Found: C, 49.79; H, 4.59; N, 3.37. SIM-MS: 733.1 $[M - I]^+$. λ_{max}, nm (ε, M^{-1} cm^{-1}): 373 (2600), 438 (2500), 556 (500).

*$CpCo(P^{Ph}{}_2N^{Ph}{}_2)I_2$ (**4**).* Yield 0.133 g (80%). ^1H NMR (300 MHz, CD_2Cl_2) δ_{ppm}: 4.12 (m, 2H), 4.30 (s, 2H), 4.55 (d, 2H), 4.72 (m, 2H), 5.51 (s, 5H), 7.05 (m, 2H), 7.05 (m, 4H), 7.28−7.53 (m, 6H), 7.72 (br, 6H), 8.05 (br, 4H). ^{31}P NMR (CD_2Cl_2): 33.3 (s) ppm. Analysis Calculated for $C_{33}H_{33}CoI_2N_2P_2$: C, 47.62; H, 4.00; N, 3.37. Found: C, 47.56; H, 4.23; N, 3.42. SIM-MS: 705.3 $[M - I]^+$. λ_{max}, nm (ε, M^{-1} cm^{-1}): 380 (2200), 438 (2400), 550 (600).

*$CpCo(dppp)I_2$ (**5**).* Yield 0.14 g (90%). ^1H NMR (300 MHz, $CDCl_3$) δ_{ppm}: 1.65 (br, 2H), 2.93 (br, 4H), 5.49 (s, 5H), 7.26−7.77 (m, 20H). ^{31}P NMR ($CDCl_3$): 27.6 (s) ppm. Analysis Calculated for $C_{32}H_{31}CoI_2P_2$: C, 48.63; H, 3.95. Found: C, 48.28; H, 4.08. SIM-MS: 663.2 (20%) $[M - I]^+$, 536.5 $[M - 2I]^+$ (45%). λ_{max}, nm (ε, M^{-1} cm^{-1}): 460 (2100), 580 (600).

General Procedure for the Synthesis of CpCo(diphosphine)-$(OTf)_2$ Compounds. A brown solution of CpCo(diphosphine)I_2 (0.05 mmol) in anhydrous CH_2Cl_2 (15 mL) was cannula-transferred into a suspension of AgOTf (38.5 mg, 0.15 mmol) in anhydrous CH_2Cl_2 (10 mL). Pale yellow precipitate of AgI formed within 5 min. After the green-brown suspension was stirred for 2 h at room temperature, the reaction mixture was filtered to remove AgI. The filtrate was evaporated under reduced pressure to yield a dark green solid. The residue was dissolved in minimum volume of dry CH_3CN (∼5 mL) and filtered via cannula to give a red solution. This solution was then layered with Et_2O (10−15 mL) and cooled to −20 °C to yield the product as red solid. X-ray quality crystals were grown by slow diffusion of Et_2O into CH_3CN or CH_2Cl_2 solution of the complex.

*$CpCo(P^{Cy}{}_2N^{Bn}{}_2)(OTf)_2$ (**6**).* Yield 63%. ^1H NMR (300 MHz, CD_3CN) δ_{ppm}: 1.28−1.60 (m, 11H), 1.83−1.91 (m, 7H), 2.39−2.46 (m, 5H), 2.74−2.84 (m, 4H), 3.14 (m, 2H), 3.31 (m, 2H), 3.72 (s, 2H), 3.91 (s, 2H), 5.71 (s, 5H), 7.12 (m, 2H), 7.35 (m, 5H), 7.48 (m, 3H), 7.71−7.83 (m, 10H). ^{31}P NMR (CD_3CN): 45.7 (s) ppm.

*$CpCo(P^{Cy}{}_2N^{Ph}{}_2)(OTf)_2$ (**7**).* Yield 70%. ^1H NMR (300 MHz, CD_3CN) δ_{ppm}: 1.30−2.15 (m, 19H), 2.46 (m, 3H), 3.01 (m, 2H), 3.26−3.30 (m, 2H), 3.62 (d, 2H), 4.01−4.08 (m, 4H), 5.87 (s, 5H), 7.12 (t, 2H), 7.25 (t, 4H), 7.56−7.41 (m, 4H), 7.71−7.83 (m, 10H). ^{31}P NMR (CD_3CN): 46.9 (s) ppm.

*$CpCo(P^{Ph}{}_2N^{Bn}{}_2)(OTf)_2$ (**8**).* Yield 65%. ^1H NMR (300 MHz, CD_3CN) δ_{ppm}: 3.02 (m, 2H), 3.15 (m, 2H), 3.44 (m, 2H), 3.74 (s, 2H), 3.90 (m, 2H), 4.18 (s, 2H), 5.50 (s, 5H), 7.08 (m, 2H), 7.32 (m, 3H), 7.52 (m, 5H), 7.71−7.83 (m, 10H). ^{31}P NMR (CD_3CN): 35.0 (s) ppm. SIM-MS/MeCN: 755.3 (100%) $[M - TfO]^+$

*$CpCo(P^{Ph}{}_2N^{Ph}{}_2)(OTf)_2$ (**9**).* **9** was precipitated from CH_2Cl_2/Et_2O mixture. Yield 78%. ^1H NMR (300 MHz, CD_2Cl_2) δ_{ppm}: 3.80 (m, 4H), 4.39 (d, 2H), 4.83 (m, 2H), 5.71 (s, 5H), 7.10−8.16 (m, 20H). ^{31}P NMR (CD_3CN): 33.5 (s) ppm. SIM-MS: 727.3 (20%) $[M - TfO]^+$, 578.4 (45%) $[M - 2TfO]^{2+}$.

*$CpCo(dppp)(OTf)_2$ (**5′**).* Yield 84%. ^1H NMR (300 MHz, CD_2Cl_2) δ_{ppm}: 2.70−2.81 (m, 6H), 5.74 (s, 5H), 7.29 (m, 4H), 7.51 (t, 4H), 7.74 (m, 12H). ^{31}P NMR (CD_2Cl_2: 30.8 (s) ppm. SIM-MS: 571.3 (100%) $[M - 2TfO + Cl]^+$.

Instruments and Methods. Electrochemical analysis was performed using a Bio-Logic science instrument SP300 potentiostat. Electrochemical experiments in DMF (tetrabutylammonium tetrafluoroborate $^nBu_4NBF_4$, 0.1 M, as the supporting electrolyte) were carried out in a three-electrode electrochemical cell using a glassy carbon working electrode (1.6 mm diameter), a platinum wire as the auxiliary electrode, and a Ag/AgCl/3 M KCl reference electrode. For electrochemical analyses, the DMF was directly used from a freshly opened bottle which contained ∼0.1−0.2% water. Only before H/D KIE studies, the DMF was dried over molecular sieves (3 Å) for 24−48 h. All potentials given in this work are reported with respect to

DOI: 10.1021/jacs.6b11474
J. Am. Chem. Soc. 2017, 139, 3685−3696

$Fc^{+/0}$ couple. The voltammograms were referenced by addition of ferrocene as an internal standard after the final experiment. The potential of the $Fc^{+/0}$ couple was found to be 0.53 V vs Ag/AgCl/3 M KCl in DMF. During CV, the solutions were degassed using solvent-saturated Ar and CO_2. Cyclic voltammograms under different partial pressure of CO_2 were recorded by sparging the solution with N_2/CO_2 gas mixtures (flow = 20 mL min^{-1}). A mass flow controller was used to mix N_2 and CO_2 in various ratios. During the electrocatalysis, aliquots of water was added using a gastight Hamilton syringe (1% v/v water/DMF = 0.56 M water in DMF). Bulk electrolysis experiments and coulometry were carried out using a mercury pool cathode with an active surface area of ~1.77 cm^2. The platinum-grid counter electrode was placed in a separate compartment connected by a glass-frit. Prior to electrolysis, the electrolyte solution was saturated with CO_2, and then the electrochemical cell was kept closed and gastight during the electrolysis. Typically the volume of electrolyte working compartment was 8 mL, and that in the counter compartment was 2 mL. Hydrogen produced during electrolysis was quantified with a PerkinElmer Clarus 500 gas chromatography equipped with a porapack Q 80/100 column (6′ × 1/8″) thermostated at 40 °C and a TCD detector thermostated at 100 °C. Carbon monoxide, methane, and other volatile hydrocarbons from the gas phase were analyzed using a flame induction detector (FID). Formic acid concentrations were determined by ionic exchange chromatography (883 Basic IC, Metrohm). UV−vis absorption spectra of compounds were recorded on an Agilent Technologies Cary 60 UV−vis spectrometer in a cuvette with 1 cm path length.

Computational Details. All calculations were carried out using TURBOMOLE (version 6.5) package.[96] Geometry optimizations of all the species have been carried out using the B3LYP functional,[97−99] complemented by the empirical dispersion scheme D3 developed by Grimme,[100] in conjunction with the def2-SV(P) basis set.[101] Considering the size of the real system, we opted for a model system where the benzyl and cyclohexyl groups are replaced by methyl groups as shown in Figure 6 in order to investigate various mechanistic options. Transition states (TS) were characterized by the presence of one and only one imaginary frequency for the desired reaction coordinate. Since the experiments were carried out using acetonitrile, the COSMO implicit solvation scheme was employed to mimic the environment.[102] Redox potentials were calculated using a thermodynamic cycle, as described elsewhere.[103] Previous studies have shown that computed redox potentials depend quite significantly on the DFT functional that was used and the solvent model that was employed (±0.35 V).[104,105] Multiple studies by Roy et al. and others have reported similar or even larger discrepancies (±0.5 V) for the calculation of redox potentials by using both hybrid and nonhybrid functionals.[106−108]

Crystal Structure Analysis: X-ray Crystallography. Diffraction data (Table S4) were collected using an Oxford Diffraction XCallibur S Kappa area detector four-circle diffractometer (Mo Kα radiation λ = 0.71073 Å, graphite monochromator), controlled by the Oxford Diffraction CrysAlis CCD software.[109] Unique intensities with $I > 10\sigma(I)$ detected on all frames using the Oxford Diffraction RED were used to refine the values of the cell parameters.

The substantial redundancy in data allows analytical absorption corrections to be applied using crystal shape determination for complex **7**, **8**, and **9′** and empirical absorption correction for complex **6**.The space group was determined from systematic absences, and it was confirmed by the successful resolution of the structure. The structure was solved by charge flipping method using superflip software for complex **7**, ShelXT direct method resolution program for complex **6** and **8**, and ShelXS for complex **9′**, in Olex1.2 environment.[109−113] All the atoms were found by difference Fourier syntheses. All non-hydrogen atoms were anisotropically refined on F2 using ShelXL program. Hydrogen atoms were fixed in ideal positions for complexes **6**, **8**, and **9′** and found by Fourier transformation and refined isotropically for complex **7**.

For complex **6**, two different orientations were found in the crystal. Twinned crystals (ratios of 0.87 and 0.13) were used to deconvoluate both contributions during the data reduction, but only the first one was taken in account for structure resolution.

CCDC 1504837 (**9′**), 1504838 (**7**), 1504839 (**6**), and 1504840 (**8**) contain the supplementary crystallographic data for this paper. These data can be obtained free of charge from the Cambridge Crystallographic Data Center via www.ccdc.cam.ac.uk/datarequest/cif. CIF files are also available as Supporting Information.

■ ASSOCIATED CONTENT

Supporting Information

The Supporting Information is available free of charge on the ACS Publications website at DOI: 10.1021/jacs.6b11474.

Calculations for TOFs/TONs and overpotentials, additional electrochemical data, DFT calculated structures and energies, and crystallographic data, including Figures S1−S29, Tables S1−S6, and Schemes S1−S3, and Cartesian coordinates of all the optimized structures for the $\mathbf{1}^{MeCN}$-Real system (PDF)

X-ray crystallographic data for **6** (CIF)

X-ray crystallographic data for **7** (CIF)

X-ray crystallographic data for **8** (CIF)

X-ray crystallographic data for **9′** (CIF)

■ AUTHOR INFORMATION

Corresponding Author

*vincent.artero@cea.fr

ORCID

Souvik Roy: 0000-0003-0146-5283

Marc Fontecave: 0000-0002-8016-4747

Phong D. Tran: 0000-0002-9561-6881

Etienne Derat: 0000-0002-8637-2707

Vincent Artero: 0000-0002-6148-8471

Present Address

#S.R.: Ångström Laboratory, Uppsala University, Lägerhyddsvägen 1, 75120 Uppsala, Sweden

Notes

The authors declare no competing financial interest.

■ ACKNOWLEDGMENTS

We acknowledge support from the French National Research Agency (ANR, Carbiored ANR-12-BS07-0024-03; Labex program ARCANE, ANR-11-LABX-0003-01 and DYNAMO, ANR-11-LABX-0011) and from Fondation de l'Orangerie for individual philanthropy and its donors.

■ REFERENCES

(1) Appel, A. M.; Bercaw, J. E.; Bocarsly, A. B.; Dobbek, H.; DuBois, D. L.; Dupuis, M.; Ferry, J. G.; Fujita, E.; Hille, R.; Kenis, P. J. A.; Kerfeld, C. A.; Morris, R. H.; Peden, C. H. F.; Portis, A. R.; Ragsdale, S. W.; Rauchfuss, T. B.; Reek, J. N. H.; Seefeldt, L. C.; Thauer, R. K.; Waldrop, G. L. *Chem. Rev.* **2013**, *113*, 6621.

(2) Qiao, J. L.; Liu, Y. Y.; Hong, F.; Zhang, J. J. *Chem. Soc. Rev.* **2014**, *43*, 631.

(3) Costentin, C.; Robert, M.; Saveant, J. M. *Chem. Soc. Rev.* **2013**, *42*, 2423.

(4) Rakowski Dubois, M.; Dubois, D. L. *Acc. Chem. Res.* **2009**, *42*, 1974.

(5) Takeda, H.; Cometto, C.; Ishitani, O.; Robert, M. *ACS Catal.* **2017**, *7*, 70.

(6) Taheri, A.; Berben, L. A. *Chem. Commun.* **2016**, *52*, 1768.

(7) Verma, S.; Kim, B.; Jhong, H. R.; Ma, S.; Kenis, P. J. *ChemSusChem* **2016**, *9*, 1972.

(8) Schmidt, I.; Müller, K.; Arlt, W. *Energy Fuels* **2014**, *28*, 6540.

DOI: 10.1021/jacs.6b11474
J. Am. Chem. Soc. 2017, 139, 3685−3696

(9) Mellmann, D.; Sponholz, P.; Junge, H.; Beller, M. *Chem. Soc. Rev.* **2016**, *45*, 3954.
(10) Yu, X.; Pickup, P. G. *J. Power Sources* **2008**, *182*, 124.
(11) Li, H.; Opgenorth, P. H.; Wernick, D. G.; Rogers, S.; Wu, T.-Y.; Higashide, W.; Malati, P.; Huo, Y.-X.; Cho, K. M.; Liao, J. C. *Science* **2012**, *335*, 1596.
(12) Mondal, B.; Song, J.; Neese, F.; Ye, S. *Curr. Opin. Chem. Biol.* **2015**, *25*, 103.
(13) Reda, T.; Plugge, C. M.; Abram, N. J.; Hirst, J. *Proc. Natl. Acad. Sci. U. S. A.* **2008**, *105*, 10654.
(14) Mota, C. S.; Rivas, M. G.; Brondino, C. D.; Moura, I.; Moura, J. J. G.; González, P. J.; Cerqueira, N. M. F. S. A. *JBIC, J. Biol. Inorg. Chem.* **2011**, *16*, 1255.
(15) Dobbek, H.; Svetlitchnyi, V.; Gremer, L.; Huber, R.; Meyer, O. *Science* **2001**, *293*, 1281.
(16) Dobbek, H.; Gremer, L.; Kiefersauer, R.; Huber, R.; Meyer, O. *Proc. Natl. Acad. Sci. U. S. A.* **2002**, *99*, 15971.
(17) Lubitz, W.; Ogata, H.; Rüdiger, O.; Reijerse, E. *Chem. Rev.* **2014**, *114*, 4081.
(18) Simmons, T. R.; Berggren, G.; Bacchi, M.; Fontecave, M.; Artero, V. *Coord. Chem. Rev.* **2014**, *270−271*, 127.
(19) DuBois, D. L. *Inorg. Chem.* **2014**, *53*, 3935.
(20) Shaw, W. J.; Helm, M. L.; DuBois, D. L. *Biochim. Biophys. Acta, Bioenerg.* **2013**, *1827*, 1123.
(21) Dutta, A.; Lense, S.; Hou, J.; Engelhard, M. H.; Roberts, J. A. S.; Shaw, W. J. *J. Am. Chem. Soc.* **2013**, *135*, 18490.
(22) Dutta, A.; DuBois, D. L.; Roberts, J. A. S.; Shaw, W. J. *Proc. Natl. Acad. Sci. U. S. A.* **2014**, *111*, 16286.
(23) Rodriguez-Macia, P.; Dutta, A.; Lubitz, W.; Shaw, W. J.; Rudiger, O. *Angew. Chem., Int. Ed.* **2015**, *54*, 12303.
(24) Seu, C. S.; Appel, A. M.; Doud, M. D.; DuBois, D. L.; Kubiak, C. P. *Energy Environ. Sci.* **2012**, *5*, 6480.
(25) Schneider, J.; Jia, H.; Kobiro, K.; Cabelli, D. E.; Muckerman, J. T.; Fujita, E. *Energy Environ. Sci.* **2012**, *5*, 9502.
(26) Song, J.; Klein, E. L.; Neese, F.; Ye, S. *Inorg. Chem.* **2014**, *53*, 7500.
(27) Costentin, C.; Drouet, S.; Robert, M.; Saveant, J. M. *Science* **2012**, *338*, 90.
(28) Costentin, C.; Robert, M.; Savéant, J.-M.; Tatin, A. *Proc. Natl. Acad. Sci. U. S. A.* **2015**, *112*, 6882.
(29) Chapovetsky, A.; Do, T. H.; Haiges, R.; Takase, M. K.; Marinescu, S. C. *J. Am. Chem. Soc.* **2016**, *138*, 5765.
(30) Ahn, S. T.; Bielinski, E. A.; Lane, E. M.; Chen, Y.; Bernskoetter, W. H.; Hazari, N.; Palmore, G. T. R. *Chem. Commun.* **2015**, *51*, 5947.
(31) Zhang, Y.; MacIntosh, A. D.; Wong, J. L.; Bielinski, E. A.; Williard, P. G.; Mercado, B. Q.; Hazari, N.; Bernskoetter, W. H. *Chem. Sci.* **2015**, *6*, 4291.
(32) Lilio, A. M.; Reineke, M. H.; Moore, C. E.; Rheingold, A. L.; Takase, M. K.; Kubiak, C. P. *J. Am. Chem. Soc.* **2015**, *137*, 8251.
(33) Bays, J. T.; Priyadarshani, N.; Jeletic, M. S.; Hulley, E. B.; Miller, D. L.; Linehan, J. C.; Shaw, W. J. *ACS Catal.* **2014**, *4*, 3663.
(34) Bielinski, E. A.; Förster, M.; Zhang, Y.; Bernskoetter, W. H.; Hazari, N.; Holthausen, M. C. *ACS Catal.* **2015**, *5*, 2404.
(35) Bielinski, E. A.; Lagaditis, P. O.; Zhang, Y.; Mercado, B. Q.; Würtele, C.; Bernskoetter, W. H.; Hazari, N.; Schneider, S. *J. Am. Chem. Soc.* **2014**, *136*, 10234.
(36) Borovik, A. S. *Acc. Chem. Res.* **2005**, *38*, 54.
(37) Shook, R. L.; Peterson, S. M.; Greaves, J.; Moore, C.; Rheingold, A. L.; Borovik, A. S. *J. Am. Chem. Soc.* **2011**, *133*, 5810.
(38) Rigsby, M. L.; Wasylenko, D. J.; Pegis, M. L.; Mayer, J. M. *J. Am. Chem. Soc.* **2015**, *137*, 4296.
(39) Fraze, K.; Wilson, A. D.; Appel, A. M.; Rakowski DuBois, M.; DuBois, D. L. *Organometallics* **2007**, *26*, 3918.
(40) Wilson, A. D.; Newell, R. H.; McNevin, M. J.; Muckerman, J. T.; Rakowski DuBois, M.; DuBois, D. L. *J. Am. Chem. Soc.* **2006**, *128*, 358.
(41) Galan, B. R.; Schöffel, J.; Linehan, J. C.; Seu, C.; Appel, A. M.; Roberts, J. A. S.; Helm, M. L.; Kilgore, U. J.; Yang, J. Y.; DuBois, D. L.; Kubiak, C. P. *J. Am. Chem. Soc.* **2011**, *133*, 12767.
(42) Wilson, A. D.; Newell, R. H.; McNevin, M. J.; Muckerman, J. T.; DuBois, M. R.; DuBois, D. L. *J. Am. Chem. Soc.* **2006**, *128*, 358.
(43) Fang, M.; Wiedner, E. S.; Dougherty, W. G.; Kassel, W. S.; Liu, T.; DuBois, D. L.; Bullock, R. M. *Organometallics* **2014**, *33*, 5820.
(44) Gennaro, A.; Isse, A. A.; Vianello, E. *J. Electroanal. Chem. Interfacial Electrochem.* **1990**, *289*, 203.
(45) Kaeffer, N.; Morozan, A.; Fize, J.; Martinez, E.; Guetaz, L.; Artero, V. *ACS Catal.* **2016**, *6*, 3727.
(46) Anxolabéhère-Mallart, E.; Costentin, C.; Fournier, M.; Nowak, S.; Robert, M.; Savéant, J.-M. *J. Am. Chem. Soc.* **2012**, *134*, 6104.
(47) Saveant, J. M. *Chem. Rev.* **2008**, *108*, 2348.
(48) Costentin, C.; Drouet, S.; Robert, M.; Savéant, J.-M. *J. Am. Chem. Soc.* **2012**, *134*, 11235.
(49) Under such conditions, only 38% of the current corresponds to formic acid production.
(50) Chen, L.; Guo, Z.; Wei, X.-G.; Gallenkamp, C.; Bonin, J.; Anxolabéhère-Mallart, E.; Lau, K.-C.; Lau, T.-C.; Robert, M. *J. Am. Chem. Soc.* **2015**, *137*, 10918.
(51) Huan, T. N.; Andreiadis, E. S.; Heidkamp, J.; Simon, P.; Derat, E.; Cobo, S.; Royal, G.; Bergmann, A.; Strasser, P.; Dau, H.; Artero, V.; Fontecave, M. *J. Mater. Chem. A* **2015**, *3*, 3901.
(52) The −1. 35 V vs Fc^+/Fc value initially determined in ref 44 was refined to that value by taking the value published for the equilibrium potential in water: Fujita, E. *Coord. Chem. Rev.* **1999**, *185−186*, 373.
(53) Costentin, C.; Passard, G.; Robert, M.; Savéant, J.-M. *Proc. Natl. Acad. Sci. U. S. A.* **2014**, *111*, 14990.
(54) Kang, P.; Cheng, C.; Chen, Z.; Schauer, C. K.; Meyer, T. J.; Brookhart, M. *J. Am. Chem. Soc.* **2012**, *134*, 5500.
(55) Kang, P.; Meyer, T. J.; Brookhart, M. *Chem. Sci.* **2013**, *4*, 3497.
(56) Taheri, A.; Thompson, E. J.; Fettinger, J. C.; Berben, L. A. *ACS Catal.* **2015**, *5*, 7140.
(57) Taheri, A.; Berben, L. A. *Inorg. Chem.* **2016**, *55*, 378.
(58) Rail, M. D.; Berben, L. A. *J. Am. Chem. Soc.* **2011**, *133*, 18577.
(59) Koelle, U.; Paul, S. *Inorg. Chem.* **1986**, *25*, 2689.
(60) Wiedner, E. S.; Bullock, R. M. *J. Am. Chem. Soc.* **2016**, *138*, 8309.
(61) DFT calculations do not evidence any interaction between a cobalt(III)-hydride species and CO_2, even in the presence of water.
(62) Schuster, C. H.; Diao, T.; Pappas, I.; Chirik, P. J. *ACS Catal.* **2016**, *6*, 2632.
(63) Obligacion, J. V.; Bezdek, M. J.; Chirik, P. J. *J. Am. Chem. Soc.* **2017**, DOI: 10.1021/jacs.6b13346.
(64) Muckerman, J. T.; Skone, J. H.; Ning, M.; Wasada-Tsutsui, Y. *Biochim. Biophys. Acta, Bioenerg.* **2013**, *1827*, 882.
(65) Izutsu, K. *Acid-Base Dissociation Constants in Dipolar Aprotic Solvents*; Blackwell Scientific: Oxford, UK, 1990.
(66) Schneider, J.; Jia, H.; Muckerman, J. T.; Fujita, E. *Chem. Soc. Rev.* **2012**, *41*, 2036.
(67) Chen, X.; Jing, Y.; Yang, X. *Chem. - Eur. J.* **2016**, *22*, 8897.
(68) Jeletic, M. S.; Mock, M. T.; Appel, A. M.; Linehan, J. C. *J. Am. Chem. Soc.* **2013**, *135*, 11533.
(69) Zall, C. M.; Linehan, J. C.; Appel, A. M. *ACS Catal.* **2015**, *5*, 5301.
(70) Bagherzadeh, S.; Mankad, N. P. *J. Am. Chem. Soc.* **2015**, *137*, 10898.
(71) Galan, B. R.; Reback, M. L.; Jain, A.; Appel, A. M.; Shaw, W. J. *Eur. J. Inorg. Chem.* **2013**, *2013*, 5366.
(72) Lim, C.-H.; Holder, A. M.; Hynes, J. T.; Musgrave, C. B. *J. Am. Chem. Soc.* **2014**, *136*, 16081.
(73) Lim, C.-H.; Holder, A. M.; Hynes, J. T.; Musgrave, C. B. *J. Phys. Chem. Lett.* **2015**, *6*, 5078.
(74) Riduan, S. N.; Zhang, Y.; Ying, J. Y. *Angew. Chem., Int. Ed.* **2009**, *48*, 3322.
(75) Chakraborty, S.; Zhang, J.; Krause, J. A.; Guan, H. *J. Am. Chem. Soc.* **2010**, *132*, 8872.
(76) Courtemanche, M.-A.; Légaré, M.-A.; Maron, L.; Fontaine, F.-G. *J. Am. Chem. Soc.* **2014**, *136*, 10708.
(77) Ménard, G.; Stephan, D. W. *J. Am. Chem. Soc.* **2010**, *132*, 1796.

DOI: 10.1021/jacs.6b11474
J. Am. Chem. Soc. 2017, 139, 3685−3696

(78) Smieja, J. M.; Benson, E. E.; Kumar, B.; Grice, K. A.; Seu, C. S.; Miller, A. J. M.; Mayer, J. M.; Kubiak, C. P. *Proc. Natl. Acad. Sci. U. S. A.* **2012**, *109*, 15646.
(79) Costentin, C.; Drouet, S.; Passard, G.; Robert, M.; Savéant, J.-M. *J. Am. Chem. Soc.* **2013**, *135*, 9023.
(80) Slater, S.; Wagenknecht, J. H. *J. Am. Chem. Soc.* **1984**, *106*, 5367.
(81) Bolinger, C. M.; Sullivan, B. P.; Conrad, D.; Gilbert, J. A.; Story, N.; Meyer, T. J. *J. Chem. Soc., Chem. Commun.* **1985**, 796.
(82) Ishida, H.; Tanaka, H.; Tanaka, K.; Tanaka, T. *J. Chem. Soc., Chem. Commun.* **1987**, 131.
(83) Ishida, H.; Tanaka, K.; Tanaka, T. *Organometallics* **1987**, *6*, 181.
(84) Bolinger, C. M.; Story, N.; Sullivan, B. P.; Meyer, T. J. *Inorg. Chem.* **1988**, *27*, 4582.
(85) Collin, J. P.; Jouaiti, A.; Sauvage, J. P. *Inorg. Chem.* **1988**, *27*, 1986.
(86) Caix, C.; Chardon-Noblat, S.; Deronzier, A. *J. Electroanal. Chem.* **1997**, *434*, 163.
(87) Pun, S.-N.; Chung, W.-H.; Lam, K.-M.; Guo, P.; Chan, P.-H.; Wong, K.-Y.; Che, C.-M.; Chen, T.-Y.; Peng, S.-M. *J. Chem. Soc., Dalton Trans.* **2002**, 575.
(88) Machan, C. W.; Sampson, M. D.; Kubiak, C. P. *J. Am. Chem. Soc.* **2015**, *137*, 8564.
(89) Witt, S. E.; White, T. A.; Li, Z.; Dunbar, K. R.; Turro, C. *Chem. Commun.* **2016**, *52*, 12175.
(90) Franco, F.; Cometto, C.; Ferrero Vallana, F.; Sordello, F.; Priola, E.; Minero, C.; Nervi, C.; Gobetto, R. *Chem. Commun.* **2014**, *50*, 14670.
(91) Wiedner, E. S.; Chambers, M. B.; Pitman, C. L.; Bullock, R. M.; Miller, A. J. M.; Appel, A. M. *Chem. Rev.* **2016**, *116*, 8655.
(92) Ginovska-Pangovska, B.; Dutta, A.; Reback, M. L.; Linehan, J. C.; Shaw, W. J. *Acc. Chem. Res.* **2014**, *47*, 2621.
(93) Coutard, N.; Kaeffer, N.; Artero, V. *Chem. Commun.* **2016**, *52*, 13728.
(94) Märkl, V. G.; Jin, G. Y.; Schoerner, C. *Tetrahedron Lett.* **1980**, *21*, 1409.
(95) King, R. B. *Inorg. Chem.* **1966**, *5*, 82.
(96) Furche, F.; Ahlrichs, R.; Hättig, C.; Klopper, W.; Sierka, M.; Weigend, F. *WIREs Comput. Mol. Sci.* **2014**, *4*, 91.
(97) Becke, A. D. *Phys. Rev. A: At., Mol., Opt. Phys.* **1988**, *38*, 3098.
(98) Lee, C.; Yang, W.; Parr, R. G. *Phys. Rev. B: Condens. Matter Mater. Phys.* **1988**, *37*, 785.
(99) Becke, A. D. *J. Chem. Phys.* **1993**, *98*, 5648.
(100) Grimme, S.; Antony, J.; Ehrlich, S.; Krieg, H. *J. Chem. Phys.* **2010**, *132*, 154104.
(101) Weigend, F.; Ahlrichs, R. *Phys. Chem. Chem. Phys.* **2005**, *7*, 3297.
(102) Klamt, A.; Schuurmann, G. *J. Chem. Soc., Perkin Trans. 2* **1993**, 799.
(103) Roy, L. E.; Jakubikova, E.; Guthrie, M. G.; Batista, E. R. *J. Phys. Chem. A* **2009**, *113*, 6745.
(104) Bhattacharjee, A.; Andreiadis, E. S.; Chavarot-Kerlidou, M.; Fontecave, M.; Field, M. J.; Artero, V. *Chem. - Eur. J.* **2013**, *19*, 15166.
(105) Canaguier, S.; Fourmond, V.; Perotto, C. U.; Fize, J.; Pecaut, J.; Fontecave, M.; Field, M. J.; Artero, V. *Chem. Commun.* **2013**, *49*, 5004.
(106) Roy, L. E.; Batista, E. R.; Hay, P. J. *Inorg. Chem.* **2008**, *47*, 9228.
(107) Roy, L. E.; Jakubikova, E.; Guthrie, M. G.; Batista, E. R. *J. Phys. Chem. A* **2009**, *113*, 6745.
(108) Reiher, M.; Salomon, O.; Hess, B. A. *Theor. Chem. Acc.* **2001**, *107*, 48.
(109) Palatinus, L.; Chapuis, G. *J. Appl. Crystallogr.* **2007**, *40*, 786.
(110) Dolomanov, O. V.; Bourhis, L. J.; Gildea, R. J.; Howard, J. A. K.; Puschmann, H. *J. Appl. Crystallogr.* **2009**, *42*, 339.
(111) Sheldrick, G. *Acta Crystallogr., Sect. A: Found. Crystallogr.* **2008**, *64*, 112.
(112) Sheldrick, G. M. *Acta Crystallogr., Sect. A: Found. Adv.* **2015**, *A71*, 3.
(113) Sheldrick, G. M. *Acta Crystallogr., Sect. C: Struct. Chem.* **2015**, *C71*, 3.

DOI: 10.1021/jacs.6b11474
J. Am. Chem. Soc. 2017, 139, 3685−3696